

# A Fully-Focused SAR Omega-K Closed-Form Algorithm for the Sentinel-6 Radar Altimeter: Methodology and Applications

Sergi Hernández-Burgos, Ferran Gibert, Antoni Broquetas, Marcel Kleinherenbrink, Adrián Flores De la Cruz, Adrià Gómez-Olivé, Albert Garcia-Mondéjar and Mònica Roca i Aparici

**Abstract**—The two-dimensional frequency-based omega-K method is known to be a suitable algorithm for Fully-Focused SAR (FF-SAR) radar altimeter processors, as its computational efficiency is much higher than equivalent time-based alternatives without much performance degradation. In this paper we provide a closed-form description of a two-dimensional frequency domain omega-K algorithm specific for instruments such as Poseidon-4 onboard Sentinel-6. The processor is validated with real data from point targets and over open ocean. Applications such as ocean swell retrieval and lead detection are demonstrated, showing the potentiality of the processor for future operational global-scale products.

**Index Terms**—Altimetry, synthetic aperture radar (SAR), delay/Doppler altimetry, SAR altimetry, Fully-Focused SAR, omega-K

## I. INTRODUCTION

SPACE-BASED radar altimetry has become nowadays a consolidated Earth Observation technique with a wide range of applications, such as estimating water surface elevations in coastal and inland waters [1], monitoring and forecasting river discharges and extreme flood events [2], studying the changes in snow, ice height and sea-ice elevation in Antarctica [3], [4], estimating the contribution of ice melting to the sea level rise [5], or mapping ice elevation and elevation change using swath interferometry altimetry [6], among others.

One of the limitations of conventional radar altimeters is the along-track resolution, which is the ability to distinguish between two targets along the surface. Initial pulse-limited radar altimeters had an along-track resolution of the size of the pulse-limited footprint, that is several kilometers [7]. In modern missions like CryoSat-2 [8], Sentinel-3 [9], or Sentinel-6 [10], this kilometer scale limitation has been overcome by transmitting pulses at high repetition frequency ensuring

This work was supported by the Industrial Doctorates Plan from the Secretary of Universities and Research of the Department of Business and Knowledge of the Government of Catalonia, under the grant Doctorats Industrials 2020, under project SA.45217 with expedient number 094. (*Corresponding author: Sergi Hernández Burgos.*)

Sergi Hernández Burgos is with isardSAT, S.L., 08042 Barcelona, Catalonia and Universitat Politècnica de Catalunya, 08034 Barcelona, Catalonia. (e-mail: sergi.hernandez@isardsat.cat).

Ferran Gibert, Adrián Flores De la Cruz, Adrià Gómez-Olivé, Albert Garcia-Mondéjar and Mònica Roca i Aparici are with isardSAT, S.L., 08042 Barcelona, Catalonia.

Antoni Broquetas is with Universitat Politècnica de Catalunya, 08034 Barcelona, Catalonia.

Marcel Kleinherenbrink is with Technische Universiteit Delft, 2628 CD Delft, Netherlands.

coherence among them, allowing for a significant increase in the number of independent looks obtained from a single scatterer on Earth, thus enabling for Doppler-based beam-forming analysis and achieving resolutions below the kilometer scale [11]. This technological advancement allows for more accurate measurements of the Earth's surface features.

First generation of altimeters using high Pulse Repetition Frequency (PRF) operate in closed-burst, meaning that they send groups of pulses and then await for their complete reception before sending the next burst. Indeed, missions such as CryoSat-2 or Sentinel-3 operate in this way with a PRF of 19 kHz. Applying a delay/Doppler processor (DDP) [11], closed-burst processing of 64 pulses leads to azimuth resolutions of approximately 300 m for missions such as CryoSat-2 and Sentinel-3. Newer missions, such as Sentinel-6, employ a nearly continuous pulse transmission approach with a PRF of 9-10 kHz [12], what allows to operate in an interleaved mode and eliminates the necessity of grouping pulses into bursts [13], though its high resolution operational processor is still based on delay/Doppler. The interleaved mode maximizes the measurement precision while ensuring a connection between data from prior altimeter missions [14], [15]. It also increases the effective PRF with respect to the closed-burst mode, reducing considerably the number of replicas that appear along-track [16].

In 2017, A. Egido and W.H.F. Smith introduced the Fully-Focused SAR (FF-SAR) backprojection algorithm (FF-BP), which can achieve along-track resolutions of up to the theoretical maximum, approximately half the length of the antenna in the flight direction (i.e. approximately 0.5 m for Sentinel-6) [17]. While this algorithm results in an improvement of the spatial resolution of the altimeter radargram, it also comes with high execution times. Still, such algorithm allowed to improve altimeter performance over some applications such inland waters [18], [19] and coastal areas [20], [21], [22], also opening the door to new calibration techniques applications [23]. Faster backprojection algorithms have been introduced for traditional SAR systems [24], [25], yet their applicability to radar altimetry remains unexplored and requires further investigation.

In 2018, Guccione et al. presented the 2D Frequency Domain FF-SAR algorithm, introducing a numerical solution based on the omega-K algorithm typically used in SAR imaging for the specific case of the CryoSat-2 radar altimeter, improving the computational efficiency of the FF-SAR

backprojection algorithm while maintaining the same level of along-track resolution [26]. Also in 2018, Scagliola et al. presented a FF-SAR frequency domain approach based in the range-Doppler algorithm used in SAR imaging [27].

In this article we continue exploring the two-dimensional frequency algorithm based in the omega-K from SAR imaging for the Sentinel-6 mission, introducing a closed-form filter by assuming an hyperbolic range with respect to one scatterer, as well as making certain orbit linear assumptions, which are further explained in the methodology section. Indeed, this paper aims at providing a comprehensive explanation of the mathematical development required to derive the final expression of focused single-look (SL) waveforms for ideal point targets. The central focus is to demonstrate that, when ideal conditions are met, the final expression of focused single-look waveforms is equivalent to the form derived through a backprojection processor, without significant precision loss while reducing drastically the execution time. Furthermore, the results obtained show the robustness of the proposed algorithm with real data, including point targets and open ocean scenarios.

The enhanced computational efficiency of the algorithm presented, along with its ability to maintain high resolution, makes it an interesting solution for applications that require improved along-track resolution with respect DDP techniques but also processing global-scale amount of data. Indeed, this advancement empowers the algorithm to produce local and global FF-SAR products for both scientific research and operational utilization. Since time-domain processors such as backprojection requires prolonged execution durations for computing global-scale products, the FF-SAR omega-K algorithm (FF-WK) emerges as a valuable alternative. In particular, applications such as swell monitoring [28] and lead detection [29] may benefit from these algorithms.

We commence with a methodology section elaborating the mathematical derivation of the FF-SAR omega-K algorithm. The subsequent section shows the practical implementation details of the algorithm. After that, we evaluate the algorithm's performance through extensive validation in a dedicated section over point and distributed targets. Moving forward, the results section follows, presenting the possible applications of the algorithm within real-world scenarios, such as swell retrieval for open ocean and lead detection for sea ice. The results section also shows a comparative in terms of computational efficiency between the omega-K and the FF-SAR backprojection algorithm. Following that, we discuss potential future research directions that can build upon the algorithm proposed. Lastly, the paper concludes with a section summarizing our findings and offering conclusions.

## II. RADAR ALTIMETRY THEORY

The omega-K algorithm is a well-known technique employed in SAR imaging to reduce the number of operations with respect to backprojection by making certain assumptions about orbit geometry (such as the hyperbolic range equation or constant nominal velocity) and the transmitted signal characteristics of the satellite [30]. Its key step involves

employing the Fourier Transform to manipulate the frequency domain in both the range and along-track dimensions, using the coherence of the radar pulses to filter a large block of echoes at once. Instead, backprojection applies filtering for each scatterer defined in a grid, incrementing substantially the number of operations needed to filter an entire surface. In this section, we present the mathematical formulation and implementation details of the omega-K algorithm tailored for the altimeter case, which shares similarities with SAR imaging missions but incorporates some design differences, such as wider synthetic apertures, nadir-pointing antenna, higher carrier frequencies, and higher pulse bandwidth. By delving into the information provided in this section, readers should gain a comprehensive understanding of the omega-K algorithm and its applications in radar altimetry. Subsequent sections will discuss the algorithm's effectiveness and performance, accompanied by the presentation of results.

### A. Transmitted and received signal

For technical and processing reasons, most high range resolution radars, including altimeters, transmit chirp pulses [31], as described by the following equation:

$$s_t(t) = w_t(t) \cos \left[ 2\pi \left( f_c t - \frac{\alpha}{2} t^2 \right) \right] \quad -\frac{T_p}{2} < t < \frac{T_p}{2}. \quad (1)$$

In this equation,  $w_t(t)$  represents the pulse envelope, which is usually a rectangular window (uniform energy). Moreover,  $f_c$  is the carrier frequency of the modulated signal,  $t$  is the duration within the pulse, which is in the order of microseconds, also known as fast time, and  $\alpha$  is the chirp rate, which is defined as the ratio of the pulse bandwidth to the pulse duration:  $\alpha = B/T_p$ . The quadratic term in the phase signal is a representation of the linear frequency modulation of the pulse. After the transmission through a nadir-pointing antenna, the pulse travels to the Earth surface, where part of the energy is reflected and returned back to the sensor. We can express the received signal as

$$s_r(\eta, t) = w_\eta(\eta) w_r(t - \tau) \cdot \cos \left[ 2\pi \left( f_c(t - \tau) - \frac{\alpha}{2}(t - \tau)^2 \right) \right]. \quad (2)$$

In this equation, the received signal has a time delay proportional to twice the range  $R$  between the scatterer and the altimeter sensor  $\tau = 2R(\eta, t)/c$ , where  $c$  is the speed of light. The slow time  $\eta$  refers to the time relative to the position of the satellite and it is in the order of milliseconds. The distance between the scatterer and the altimeter sensor is influenced by the position of the satellite and the relative sensor-target movement  $R(\eta, t) \approx R(\eta) + v_r \cdot t$ . This consideration arises from our departure from the commonly used "stop and go" approximation. The "stop and go" approach assumes that the motion of the satellite is sufficiently low during the pulse duration so that it can be considered as if the satellite is stationary. In altimetry systems, this assumption cannot be sustained due to the influence of the Doppler effect in the signal phase caused by the high frequency carrier used for

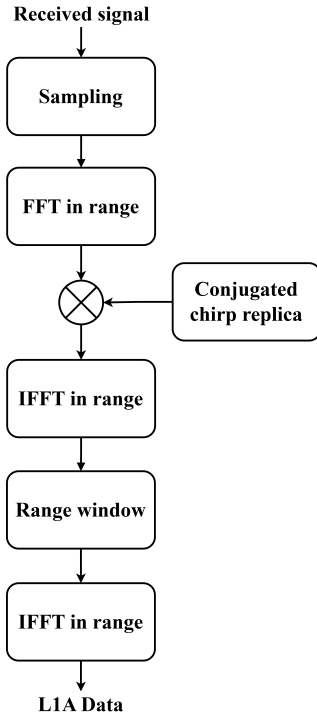


Fig. 1: On-board Sentinel-6 radar altimeter receiver system.

the altimeter [17]. This effect has also been explored in high-precision SAR for estimating Doppler parameters related to object motion [32], [33]. Furthermore, the pulse envelope  $w_r(t - \tau)$  represents the received signal energy, which is affected by physical alterations that depend on the atmosphere and the Earth's surface. The along-track envelope  $w_\eta$  is characterized for the antenna pattern.

### B. Sentinel-6 Receiver System

Figure 1 shows the processing steps of the Sentinel-6 receiver system [34]. The signal is digitised at a very high frequency (395 MHz), after which a matched filter is applied in the frequency domain using a Discrete Fourier Transform (DFT) by means of the Fast Fourier Transform algorithm (FFT). The matched filter is a conjugated replica of the transmitted pulse (chirp signal). The signal is then cut with a range window in the range-time domain, after that, an Inverse Fast Fourier Transform (IFFT) is applied.

The output signal for a single scatterer can be represented by the complex signal

$$\begin{aligned}
 S_r(\eta, f_r) = & w_\eta(\eta) W_r(f_r) \\
 & \cdot \exp \left[ -j2\pi \left( f_c \frac{2}{c} R(\eta) \right. \right. \\
 & \left. \left. - \left( \frac{2}{c} (R(\eta) - R_{trk}) - \frac{f_d}{\alpha} \right) f_r \right) \right]. \quad (3)
 \end{aligned}$$

Where  $f_r$  is the frequency variable in the range domain, known as the range frequency. Furthermore, the expression  $f_d = 2f_c v_r / c$  indicates the alteration in range of the phase due to the Doppler effect related to the relative velocity of the

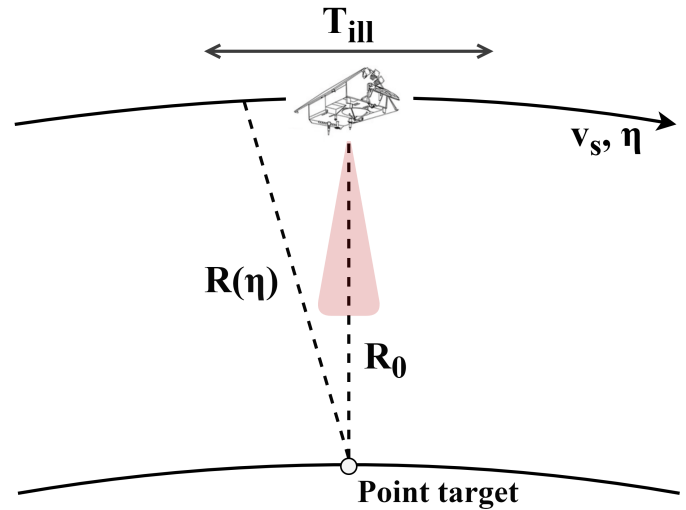


Fig. 2: Radar geometry. The satellite passes over the point target, transmitting chirp pulses periodically and receiving the echoes.

satellite. The term  $R_{trk}$  represents the tracker range, which is commanded onboard by the satellite. In the case of the Sentinel-6 altimeter, this range commonly refers to the central point within the range window. The satellite is moving while chirp pulses are periodically transmitted at a designated PRF. The motion of the satellite during the slow-time  $\eta$  results in different distances between the sensor and the scatterer for each transmitted pulse. Therefore, to accurately define the response of a target for each pulse, the range equation of the satellite with respect to the point target  $R(\eta)$  must be defined.

### C. Radar Geometry

Figure 2 illustrates a simplified geometry of a radar altimeter with a single scatterer in the scene. In order to determine the closed-form filter of the omega-K algorithm for the radar altimeter, some simplifications in the radar geometry are made: Earth is locally spherical of radius  $R_e$ , the satellite is moving along the track with a constant velocity  $v_s$ , the height of the satellite and the retracker range are constant during the entire pass. The satellite is periodically transmitting pulses during a limited illumination time,  $T_{ill}$ . When a transmitted pulse reaches the Earth's surface, part of its energy is scattered back to the sensor with a delay corresponding to the satellite-scatterer distance. The equation that defines the distance of the satellite with respect to the scatterer for each instant of time is known as the range equation. In the context of Sentinel-6, we can safely express the range equation along the x-axis as an hyperbolic form [30]:

$$R(x) \approx \sqrt{R_0^2 + x^2} \quad (4)$$

where  $R_0$  is the minimum distance between the sensor and the target. The altimeter sensor has the closest range to the scatterer when  $R(x = 0) = R_0$ . The position of the satellite  $x$  can be expressed as a function of the slow time  $\eta$  as follows:

$$x = \eta \cdot v_{eq} \quad (5)$$

where

$$v_{eq} \approx v_s \cdot \sqrt{\alpha_E} = v_s \cdot \sqrt{\frac{R_e}{(R_e + h)}}. \quad (6)$$

The equivalent speed  $v_{eq}$  is determined by multiplying the satellite's velocity  $v_s$  by a correction term to account for the curvature of the Earth, the square root of the orbital factor  $\alpha_E$  [30]. The correction term depends on the Earth's radius, denoted as  $R_e$ , and the nominal altitude of the satellite, represented as  $h$ . This velocity can also be understood as the geometric mean between the velocity of the satellite and the velocity projected on ground  $v_g$  as  $v_{eq} = \sqrt{v_s \cdot v_g}$ . With these changes of variables, the range equation becomes

$$R(\eta) = \sqrt{R_0^2 + (\eta \cdot v_{eq})^2}. \quad (7)$$

For the typical values of Sentinel-6 (Ku-band carrier frequency) and five seconds of illumination time, the difference between the approximated range and the range computed with the telemetry data is around 4 mm in the borders of the illumination time. This range equation will be further used to derive the closed form of the two-dimensional frequency signal.

#### D. Along-track Fourier Transform

In order to obtain the two-dimensional frequency signal, we need to apply the Fourier Transform in the slow time (along-track) domain to the received signal (3):

$$S(f_\eta, f_r) = \int_{-\infty}^{\infty} S_r(\eta, f_r) \exp[-j2\pi\eta f_\eta] d\eta \quad (8)$$

$S(f_\eta, f_r)$  is the two-dimensional frequency signal where  $f_\eta$  is the along-track frequency variable. This frequency variable is also called Doppler frequency. Regarding the phase of the integral, it contains quadratic terms in the slow time variable, making it challenging to obtain an analytical expression. Nevertheless, we can overcome this obstacle by applying the Principle of Stationary Phase (POSP). The POSP enables us to analytically express integrals with quadratic modulation in their signal by locating the stationary phase point  $\eta_0$  where the derivative of the phase of the integral is zero [35]. Consequently, the whole phase that requires derivation is

$$\theta(\eta) = f_c \frac{2}{c} R(\eta) - \left( \frac{2}{c} (R(\eta) - R_{trk}) - \frac{f_d(\eta)}{\alpha} \right) f_r - \eta f_\eta. \quad (9)$$

The stationary phase point  $\eta_0$  can be obtained by finding the zero in the derivative of the phase defined in the latter equation

$$\left. \frac{\partial \theta(\eta)}{\partial \eta} \right|_{\eta=\eta_0} = 0 \quad (10)$$

Once we obtain the stationary phase point  $\eta_0$ , the two-dimensional frequency signal can be expressed as

$$S(f_\eta, f_r) \approx w_\eta(\eta_0) \cdot W_r(f_r) \cdot \exp[-j2\pi \cdot \theta(\eta_0)] \quad (11)$$

The along-track frequency domain envelope is obtained by substituting the stationary phase point  $\eta_0$  to the along-track time domain envelope. The two-dimensional frequency phase is obtained by substituting the stationary phase point  $\eta_0$  into the whole phase defined in (9). Note that the stationary phase point is a function of the range frequency and Doppler frequency. To enhance clarity, we have omitted residual terms arising from the POSP assumption, as they are deemed to be of negligible significance [26].

#### E. Stationary Phase Point

To obtain a closed form expression of the two-dimensional frequency signal (11), we must obtain the derivative of the whole phase (9)

$$(f_c - f_r) \frac{2}{c} \frac{\partial R(\eta)}{\partial \eta} + \frac{1}{\alpha} \frac{\partial f_d(\eta)}{\partial \eta} f_r - f_\eta = 0. \quad (12)$$

As explained in Section II-C, we will use an hyperbolic range equation for  $R(\eta)$ . Moreover, the Doppler frequency shift  $f_d(\eta)$  will be represented as a linear function of the slow time  $f_d(\eta) = \beta_d \cdot \eta$  as in [26]. By performing the derivative in (12), we can express that

$$(f_c - f_r) \frac{2}{c} \frac{v_{eq}^2 \eta}{\sqrt{R_0^2 + (v_{eq} \cdot \eta)^2}} + \frac{\beta_d}{\alpha} f_r - f_\eta = 0. \quad (13)$$

In previous work [26], the equation (13) is presented for the CryoSat-2 case [26, Eq. 8]. However, in the publication no more details are provided after this point, leaving the equation as an intermediate form without providing a closed form expression. Instead, they propose a numerical approach to determine the stationary phase point  $\eta_0$  by calculating the roots directly in (12). This eliminates the need for making various simplifications listed earlier, such as the hyperbolic range. In contrast, the closed-form filter needs fewer computational operations and requires less memory load. It also reduces the complexity of the processor design. Moreover, the closed-form expression enables a broader analysis of the two-dimensional frequency waveforms. It is important to remark that these assumptions can lead to a slight degradation in the accuracy of the focused point target Response (PTR), as evidenced in the results section. Building upon their findings, we present a comprehensive analysis that resolves (13) into a concise closed-form expression for the case of Sentinel-6, thereby providing a more complete understanding of its mathematical properties. Thus, after doing some algebra and isolating  $\eta$  from (13), we can express the stationary phase point  $\eta_0$  in function of the Doppler frequency  $f_\eta$  and the range frequency  $f_r$  as

$$\eta_0(f_\eta, f_r) = \frac{cR_0(f_\eta - \beta_d/\alpha \cdot f_r)}{2v_{eq}^2(f_c - f_r)} \frac{1}{D(f_\eta, f_r)}. \quad (14)$$

Where  $D(f_\eta, f_r)$  is defined as

$$D(f_\eta, f_r) = \sqrt{1 - \frac{c^2(f_\eta - \beta_d/\alpha \cdot f_r)^2}{4v_{eq}^2(f_c - f_r)^2}}. \quad (15)$$

Now we can use the stationary phase point  $\eta_0$  to determine the two-dimensional frequency signal.

#### F. Two-dimensional frequency signal for an ideal point target

After substituting the stationary phase point (14) into (9) the phase of the two-dimensional frequency signal becomes

$$\theta(\eta_0) = \frac{2}{c}(R_0(f_c - f_r) \cdot D(f_\eta, f_r) + R_{trk} \cdot f_r). \quad (16)$$

Regarding the along-track frequency envelope  $w_\eta(\eta_0)$ , the antenna pattern of the radar altimeter follows a Gaussian model [36], consequently, the illumination time is understood as the time that a target stays at 3-dB of the antenna footprint:

$$T_{ill} = 0.886 \frac{cR_0}{f_c L_a v_g} \quad (17)$$

where  $L_a$  stands by the length of the antenna in the azimuth direction. We can compensate the received energy for the antenna pattern to have a two-dimensional signal sequence of uniform energy. Thus, for an ideal point target, the two-dimensional frequency envelope can be defined as

$$W_\eta(f_\eta, f_r) \cdot W_r(f_r) \approx \Pi\left(\frac{f_\eta}{B_D}\right) \cdot \Pi\left(\frac{f_r}{B}\right). \quad (18)$$

Where  $B_D$  is the Doppler bandwidth of the point target, defined as

$$B_D = \frac{2v_{eq}^2 f_c T_{ill}}{cR_0} = 0.886 \frac{2v_s}{L_a}. \quad (19)$$

Now we can combine equations (16) and (18) to build a closed form of the two-dimensional frequency signal as defined in (11):

$$S(f_\eta, f_r) = \Pi\left(\frac{f_\eta}{B_D}\right) \cdot \Pi\left(\frac{f_r}{B}\right) \cdot \exp\left[-j \frac{4\pi}{c}(R_0 \cdot (f_c - f_r) \cdot D(f_\eta, f_r) + R_{trk} \cdot f_r)\right]. \quad (20)$$

This signal represents one target located at range  $R_0$  within the illumination time. The omega-K approach aims to apply a single filter to the two-dimensional frequency waveforms defined in the last equation. The objective is to simultaneously focus on all spatial points within a designated across-track range window and all the observed surface during a specific time period. To achieve this, a filter is constructed using a reference range  $R_{ref}$ , typically positioned at the center of the designated range window. However, it's crucial to note that residual phase contributions from spatial points around the across-track reference range could lead to defocusing. To address this concern, additional techniques like the Stolt interpolation method mentioned in [30] could be employed.

Section II-H provides an explanation for the minimal impact on defocusing surfaces whose across-track distances deviate from the reference range in altimeter systems like Sentinel-6. Within the context of the FF-SAR backprojection algorithm, the impact of applying a phase correction using one unique range for an entire range window has been already studied for the case of CryoSat-2 in [17] and [18].

#### G. Reference Function Multiply

Once we have a closed-form expression for the two-dimensional frequency signal, our objective is to correct the phase of the signal so when we come back to the two-dimensional time domain, we obtain the focused signal. To do so, we have to construct a reference function multiply (RFM), proportional to the phase of the input signal:

$$\Phi_{RFM} = \frac{2}{c}(R_{ref} \cdot (f_c - f_r) \cdot D(f_\eta, f_r) + R_{trk} \cdot f_r) \quad (21)$$

Where  $R_{ref}$  is the aforementioned reference range. Equation (21) is valid within the sampled Doppler interval  $|f_\eta| \leq PRF/2$  for the along-track frequency and the chirp bandwidth for the range frequency  $|f_r| \leq B/2$ . The reference function multiply is then multiplied by the two-dimensional frequency signal defined in (20)

$$S_{RFM} = S(f_\eta, f_r) \cdot \exp(j2\pi \cdot \Phi_{RFM}) \quad (22)$$

#### H. Two-dimensional PTR

The two-dimensional frequency signal after filtering can be expressed as

$$S_{RFM}(f_\eta, f_r, R_{ref}) = \Pi\left(\frac{f_\eta}{B_D}\right) \cdot \Pi\left(\frac{f_r}{B}\right) \cdot \exp\left[j \frac{4\pi}{c}(R_{ref} - R_0) \cdot (f_c - f_r) \cdot D(f_\eta, f_r)\right]. \quad (23)$$

When  $R_{ref} = R_0$  the phase is zero and only the envelope of the signal is left. The last step is to perform an IFFT in the along-track dimension and an FFT in the across-track dimension in order to obtain the final focused waveforms in the temporal domain. As expected, the two-dimensional response over an ideal point target is therefore a product of sinc functions:

$$s_{PT}(\eta, t) = \text{sinc}[\eta B_D] \cdot \text{sinc}[tB]. \quad (24)$$

This expression is equivalent to the signal obtained with backprojection algorithm in [17] and the signal obtained with the FF-WK numerical algorithm in [26]. Therefore, under ideal conditions, the FF-WK closed-form algorithm is equivalent to the backprojection and the FF-WK numerical algorithms. In practice, the approximations that are employed may introduce residual errors that can impact the performance in real scenarios. The validation section demonstrates that these errors are minor, leading to nearly identical focusing results.

When the reference range  $R_{ref}$  is not equal to the range of minimum approach  $R_0$ , the phase is not zero, and miss-focusing can occur. If this phase was linear with  $f_r$  and  $f_\eta$ , the signal would be focused with a delay-shift in range proportional to the linear phase, according to the well-known Fourier Shift Theorem. However, in conventional SAR systems, the term  $D(f_\eta, f_r)$  is quadratic. In order to correct this, an extra correction called Stolt interpolation is applied [30]. In an altimetry system, the carrier frequency and pulse bandwidth are typically higher than in SAR satellites. Also, the range window in altimetry is small compared to the sensor to target distance ( $\sim 93$  m for Sentinel-6 in raw SAR mode, half of it in RMC mode, for an altitude of 1336 km [34]). When comparing the term  $D(f_\eta, f_r)$  for typical SAR and altimetry systems, it is found that in SAR this term has a significant impact whereas in altimetry it does not. In the context of Sentinel-6, we are examining the phase in (23) when there is a correction error of  $R_{ref} - R_0 = 47$  meters, representing the worst-case scenario within the range window. This analysis is conducted with respect to the along-track frequency while keeping the range frequency fixed. Our observations reveal that the variation in the linear term is approximately 1 mrad. This small change is consistent enough to be treated as constant. Furthermore, when considering quadratic and higher-order terms, their variations are below 0.1 radians. This level of variation is sufficiently low to consider it negligible. Consequently, in Sentinel-6 radar altimetry, it is unnecessary to implement Stolt interpolation to focus on the remaining across-track positions. In Section IV, a PTR function comparison with and without Stolt interpolation is presented using simulated data over a point target, processed with the WK algorithm, to validate this assumption. Consequently, the range shift of the processed data projected to the focused image is proportional to the difference between the reference range and the actual point target range. We can therefore express the two-dimensional PTR as a function of the difference between the reference range and the range of minimum approach to the target as

$$s_{SL}(\eta, t) = \text{sinc}[\eta B_D] \cdot \text{sinc}[(t - \tau)B]. \quad (25)$$

$$\tau = \frac{2 \cdot (R_0 - R_{ref})}{c}. \quad (26)$$

Where constant phase terms have been omitted for the sake of simplicity.

### I. Range and Azimuth Resolution

The resolution for a sinc-shaped signal is typically defined as the width of the main lobe of the sinc at half of its maximum power [30]. Therefore, the across-track resolution is defined as

$$\delta R_\tau = 0.886 \frac{c}{2B}. \quad (27)$$

For the case of Sentinel-6, the across-track resolution is 0.415 m.

Regarding the along-track direction, the azimuth resolution in distance units is defined as:

$$\delta R_{az} = 0.886 \frac{v_g}{B_D} \gamma_w = \frac{L_a v_g}{2 v_s} \gamma_w \quad (28)$$

where  $\gamma_w$  represents a broadening factor resulting from a frequency processing window. Typically, the term  $\gamma_w v_g / v_s$  is approximated to 1, which leads to the recognized definition of azimuth resolution  $\delta R_{az} \approx L_a / 2$ .

### J. Doppler bandwidth aliasing mitigation

In the case of Sentinel-6, the Doppler bandwidth is approximately 10.6 kHz, while the PRF is 9.23 kHz. Consequently, the PRF does not meet the Nyquist theorem. The received energy from Doppler frequencies that are higher than the PRF become folded within the limits of the sampled spectrum, introducing aliasing. Figure 3 showcases the range/azimuth radargram (a) and the corresponding range/Doppler radargram (b) for a simulated point target. We can appreciate how the Doppler spectrum exhibits aliasing due to the low PRF in comparison to the Doppler bandwidth of the point target.

Over scenarios where the flat surface assumption is applicable, such as point targets, open ocean, or sea ice, a straightforward method to mitigate aliasing involves reducing the range window in order to erase aliased ranges (e.g. from 256 to 128 range samples in Fig. 3). This adjustment also helps to reduce the data rate of the satellite [37]. The primary trade-offs with this approach are the loss of information for half of the range window, which can be acceptable in open ocean and sea ice scenarios, since the most relevant information is before the range cutoff for most applications and is carefully preserved [38], [39]. Additionally, there is a loss of along-track resolution since the entire Doppler bandwidth is no longer processed. As the effective range window is reduced, the surface's range migration is constrained, consequently so as to keep the Doppler spectrum below the PRF, free of aliasing. In this case, the broadening factor is  $\gamma_w = B_D / PRF = 1.148$ , which means a loss of 14.8% in the along-track resolution with respect to the theoretical maximum. Nevertheless, as the range migration is reduced, the geometric assumptions align more closely with real data, resulting in less degradation of the PTR.

Over other kind of scenarios where the entire range window is required, such as land-ice or inland scenarios, avoiding aliased ranges through this method becomes unfeasible. In such cases, a more restrictive method involves applying a low-pass filter to the Doppler spectrum to eliminate aliased frequencies. This method, though, comes with the drawback of further reducing along-track resolution. The bandwidth of the low-pass filter is defined as

$$B_{LP} = 2PRF - B_D \quad (29)$$

For Sentinel-6 nominal parameters, the bandwidth of the low-pass filter  $B_{LP}$  is approximately 7.75 kHz, which is equivalent to a broadening factor of  $\gamma_w = B_D / B_{LP} = 1.37$ , reducing the along-track resolution by a 37% with respect to the theoretical maximum. This is valid assuming the alignment of the antenna beam's center with the point of closest approach to the target, following the orbital simplifications explained in

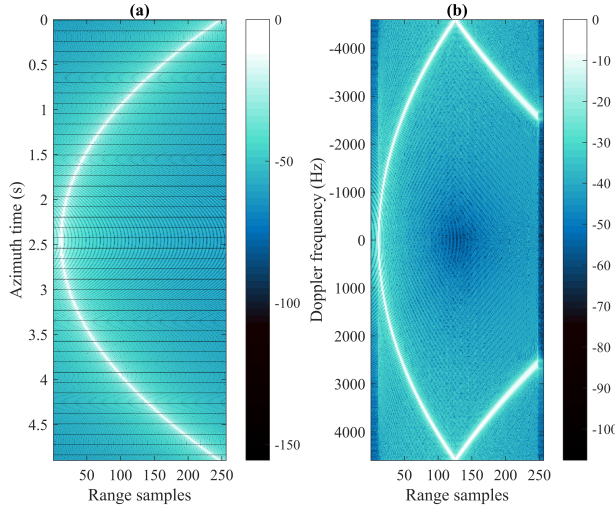


Fig. 3: 2D power radargram (dB) of a simulated point target for 4.9 s in (a) range/Azimuth domain and (b) range/Doppler domain. Due to the limited PRF, we only can process frequencies below  $PRF/2 = 4.65$  kHz. Frequencies higher than half of the PRF become folded within the limits of the sampled spectrum, appearing as interference in higher ranges.

this paper. Otherwise Doppler centroid correction techniques may be applied [30].

### III. ALGORITHM IMPLEMENTATION

In this section, we present a brief explanation of the most important points for the code implementation of the omega-K algorithm. Figure 4 provides an illustrative depiction of the overall scheme. The input data used for the omega-K processor is obtained from the Sentinel-6 Mission Copernicus Operational L1A product, formatted in NetCDF4. The received echoes in the L1A file are provided in IQ samples, organized in a three-dimensional structure, specifically in terms of bursts and samples. Each burst corresponds to 64 Ku-band echoes, followed by 1 calibration echo (CAL) and 1 C-band echo. As these CAL and C pulses serve just for calibration purposes, they need to be omitted. In practice, a gap is therefore induced every 64 science pulses. The impact on performance and potential solutions to this issue has already been described in [16] and is not assessed in this paper.

Each echo contains 256 samples where the range dimension is in frequency domain, thus only an FFT in the azimuth direction should be applied to obtain the two-dimensional frequency domain signal. Since Sentinel-6 works in interleaved mode, the PRI between bursts is usually coherent, therefore the Burst Repetition Interval (BRI) is proportional to the PRI. Telemetry data-rate is given in terms of burst intervals, so all the waveforms encapsulated in a single burst share the same satellite coordinates and time in the L1A file. The omega-K algorithm is applied to an entire block of echoes. The length of the block can be selected by the user. The construction of the RFM filter, which will be applied to the raw data, entails the calculation of the following parameters:

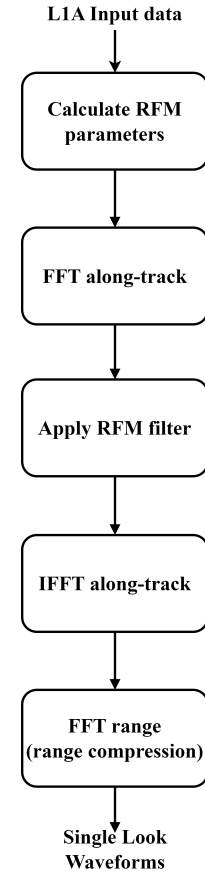


Fig. 4: Omega-K Algorithm Scheme. The input data pertains to the Sentinel-6 Mission Copernicus Operational L1A Product.

- Determine the reference range  $R_{ref}$ . Typically, the middle of the window range is selected.
- Normally, satellites exhibit a linear altitude change, introducing an additional phase term in the two-dimensional frequency signal because the closest point is not at nadir anymore. This induces a shift along the satellite direction in the projected data that can be corrected by adding a phase-shift term proportional to the altitude rate.
- Calculate the Doppler rate  $\beta_D$ . To do so, we compute the evolution of the Doppler frequency shift of the surface during all the processed time, and then calculate the slope of the resulting function.
- The effective velocity is computed by calculating the norm of the velocity vector components that are included in the L1A product. It is important to compensate the norm of the velocity by the orbital factor  $\alpha_E$ .
- The range frequency  $f_r$  is generated by creating a vector of equally spaced samples. The sampling time is available in the L1A product.
- Similarly, the along-track frequency  $f_\eta$  is generated by constructing a vector of equally spaced samples. The space between frequencies depends on the PRF, also obtainable from the L1A product.

Once these parameters are determined, the construction of the RFM filter (21) becomes possible. The RFM filter is represented as a matrix, where each column corresponds to

a range frequency and each row corresponds to an along-track frequency. Subsequently, an FFT is applied to the input waveforms in the along-track direction to obtain the two-dimensional frequency signal. Then, the RFM matrix is applied directly to the waveforms as in (22). After that, an IFFT is performed in the along-track frequency domain, followed by an FFT in the range frequency domain (also known as range compression). The output of the processor is a two-dimensional matrix of the focused surface with respect to the range. Notably, the final range window is linked to the reference range set in the RFM filter. Careful consideration of this range window is crucial to ensure accurate and meaningful results.

Another important aspect when applying an FFT in along-track is the need to have waveforms and pulses equispaced in time. For closed-burst systems like CryoSat-2 or Sentinel-3, if the BRI is not proportional to the PRI, an interpolation of the data is required to achieve equispaced waveforms among different bursts. In contrast, satellites such as Sentinel-6 operate in interleaved mode and are likely to have equispaced data during the entire processed time. Still, the PRF of such interleaved systems is dynamic as it needs to adjust to the variable satellite altitude, leading to variations in the periodicity of pulse reception throughout the illumination time. Different strategies may be employed to address such changes, such as interpolating the data to maintain a constant PRI. Moreover, it is important to know that the ignored CAL pulses induce replicas in the azimuth projection [16].

Finally, despite our emphasis on capturing all the surface visible to the satellite throughout the processed period, it is important to note the presence of transient zones at the margin of a block of echoes. These transient zones arise from the finite length of the data. Specifically, the surface at the beginning and end of the observation period do not experience full illumination. Indeed, if we consider the multiplication in the frequency domain (RFM filter) as equivalent to a convolution in time, it is clear that the output of the filter at the initial and concluding pulses is not complete, inducing edge effects. As a result, it's necessary to exclude these incompletely illuminated regions from the dataset of the radar image being focused upon.

#### IV. VALIDATION

Four different validation exercises have been considered in order to evaluate the performance of the omega-K algorithm. First, a simulator has been developed to validate the PTR of the processor against simulated data and to verify the unnecessary of the Stolt interpolation for the case of Sentinel-6. Secondly, real data from Sentinel-6 passes over a transponder and a corner reflector have been used to evaluate the real PTR and the long-term stability of the processor over point targets. Finally, an open ocean scenario is used to evaluate the performance of the processors over distributed targets. The omega-K processor used to derive all the results was developed following the steps outlined in Section III.

#### Sentinel-6 Parameters

Carrier Frequency	13.575 GHz
Pulse bandwidth	320 MHz
PRF (nominal)	9.23 kHz
Sampling Frequency (nominal)	395 MHz
Pulse duration	32 $\mu$ s
Range Samples	256
Mean Altitude	1336 km
Orbital velocity (nominal)	7.2 km/s

TABLE I: Sentinel-6 Poseidon-4 altimeter instrument parameters.

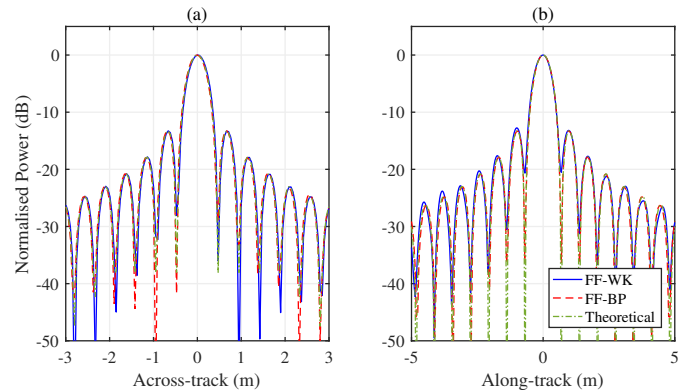


Fig. 5: Simulated PTR at the point of maximum power. FF-WK, FF-BP and theoretical model are shown. (a) Across-track cut. (b) Along-track cut.

#### A. Response over simulated point target

To validate the theoretical model and assess the performance of the algorithm, a simulated scenario has been created and analysed. This simulated data accurately replicates all stages of the Sentinel-6 receiver system, including the expected orbit and all the parameters within the Poseidon-4 altimeter instrument [10]. These parameters are outlined in Table I. Consequently, the radar geometry closely resembles an actual Sentinel-6 product. The primary advantage of employing this simulation is that the input signal for the omega-K processor can be precisely modeled according to (3). Therefore, any potential noise or interference that typically occur in real-world scenarios does not affect the performance of the algorithm. The simulated data has been processed over 3.4 seconds, which is almost the maximum we can set to apply the omega-K filter. Moreover, a zero-padding factor of 8 has been applied on the range dimension to improve visualisation. The along-track and across-track cuts for the FF-WK closed-form, FF-BP and the theoretical model are depicted in Fig. 5. It can be seen that all the signals are consistent with both FF-WK and FF-BP matching the expected theoretical model. The along-track resolution for the FF-WK closed-form method is 0.577 m, whereas for the FF-BP is 0.565 m. The expected theoretical resolution is 0.56 m, therefore, the FF-WK closed-form algorithm presents an error of 2% and the FF-BP algorithm presents an error of 1% with respect to the theoretical value.

Additionally, we utilized simulated data to assess the impact

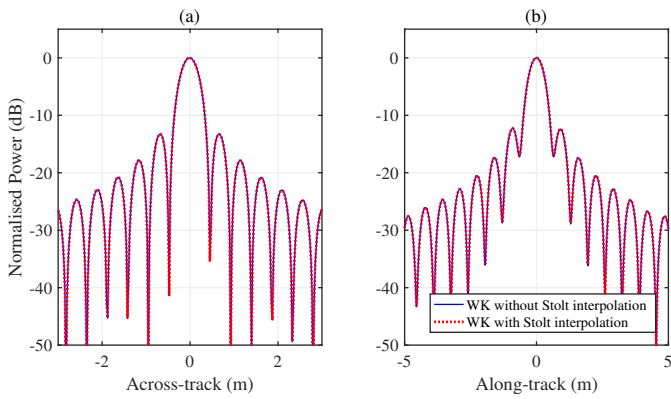


Fig. 6: Stolt Interpolation comparison: PTR at the point of maximum power. The PTR is assessed for cases when interpolation is applied and when it is not. The worst-case scenario has been evaluated, applying a reference range 47 meters away from the range of the point target. Both responses show good agreement. (a) Across-track cut. (b) Along-track cut.

of Stolt interpolation on the omega-K algorithm. For this analysis, we processed the data applying the Stolt interpolation as described in [30] and also performed the analysis without applying Stolt interpolation. Figure 6 presents a comparison of both PTR. In this case, there is a difference of 47 meters from the reference range to the real target range. This value corresponds to the maximum difference found in the Sentinel-6 range window between the center and the edges when operating in raw SAR mode, being half of it when operating in RMC mode. Notably, there is an imperceptible difference between the two cuts. Still, we have found that applying the Stolt interpolation improves the along-track resolution from 0.577 m to 0.572 m, a relative improvement of 0.87%, which we consider of negligible significance. Regarding the PSLR, differences are less than 0.1 dB.

### B. Response over real point targets

Transponders and corner reflectors are key elements for radar altimetry external calibration [40], [23]. On one hand transponders, as active elements, offer a high signal-to-noise (SNR) and signal-to-clutter (SCR) ratio compared to passive corner reflectors despite their complexity. On the other hand, passive elements such as corner-reflector are noisier but can provide very precise measurements due to their intrinsic simplicity and long-term stability. In this section, results from a single Sentinel-6 pass over a transponder are used to compare the omega-K PTR response over a point target against a backprojection algorithm and the omega-K numerical approach in [26] adapted to Sentinel-6. Moreover, results of a series of Sentinel-6 flights over a corner reflector are analysed to evaluate the long-term performance of the processor.

1) *PTR over a transponder*: Figure 7 shows the 2D PTR image from a Sentinel-6 pass on January 6, 2021, over the transponder of Crete [40], processed within 2.6 s. This duration represents the maximum observable time limited by the received power from the transponder in this pass. Figure 8 provides visualizations of the across-track and along-track sections relative to the point of maximum energy for the three

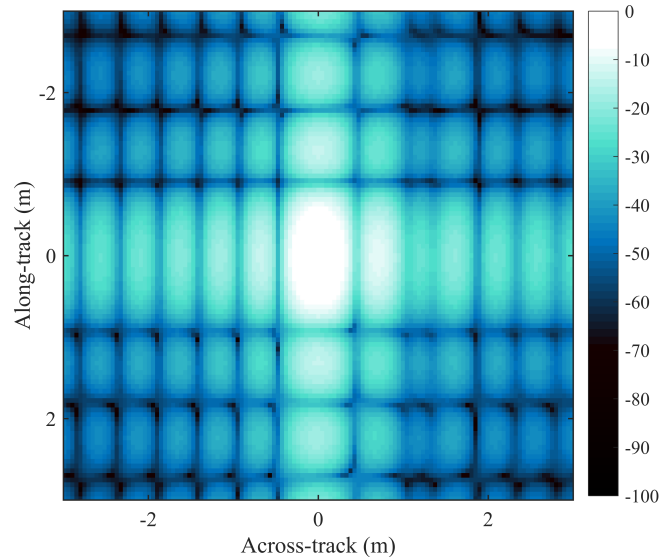


Fig. 7: FF-WK 2D PTR image corresponding to a Sentinel-6 pass on January 6, 2021 over the Crete transponder [40]. The x-axis represents the range with respect to the point target. The y-axis represents the point distance with respect to the point target. Normalised power in decibels.

processors, where the PTR response obtained by a FF-SAR backprojection processor and a FF-WK numerical processor are also plotted for comparison confirming good agreement, specially in the range case. In power terms, the peak-to-side lobe ratio (PSLR) for the across-track response measures 13.56 dB and 10 dB for the left and right lobes, respectively. Such an asymmetry, also captured by the other processors, is a well-known feature of this transponder [41]. The width of the primary lobe at -3 dB is 0.42 m, coinciding with the theoretical range resolution. The PSLR of the along-track evolution for the omega-K closed-form algorithm is 13.59 dB for the left secondary lobe and 13.95 dB for the right secondary lobe. The omega-K numerical processor presents a PSLR of 13.59 dB for the left secondary lobe and 13.4 dB for the right secondary lobe. The backprojection algorithm presents a PSLR of 14.39 dB for the left secondary lobe and 14.78 dB for the right secondary lobe. In terms of along-track resolution, the width of the main lobe is marginally broader in both omega-K processors, as the main lobe at -3 dB for the omega-K algorithm is 0.79 m, slightly wider than the theoretical resolution, which is of 0.72 m for 2.6 s of processed time. Thus, the omega-K processor has a loss in the along-track resolution of 9.7% with respect to the theoretical value. In this case, the backprojection algorithm gets closer to the theoretical value, 0.76 m with a loss of 5.6%. Refer to Table II for a comprehensive overview of all the obtained outcomes presented in this section. This table presents a summary of the results derived from the transponder outcomes using the three processors. The parameters considered in this table include across-track resolution, along-track resolution and peak-to-side lobe ratio.

2) *Range measurement stability*: The long term behaviour of the omega-K processor is assessed by evaluating its stability in terms of range measurements on a sequence of passes over

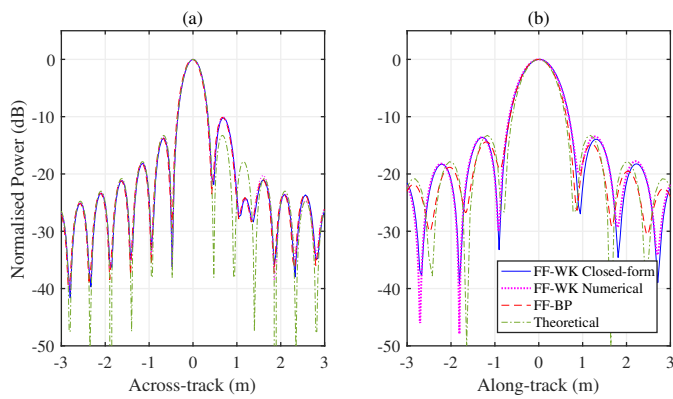


Fig. 8: PTR functions over the transponder in Crete corresponding the Sentinel-6 pass on January 6, 2021. The responses obtained by the FF-WK and FF-BP processors have been centered at the point of maximum power. (a) Across-track PTR. (b) Along-track PTR.

Transponder	FF-WK CF	FF-WK NM	FF-BP
PSLR Left Across (dB)	13.56	13.56	13.56
PSLR Right Across (dB)	10.00	10.00	10.00
PSLR Left Along (dB)	13.59	13.59	14.39
PSLR Right Along (dB)	13.95	13.40	14.78
Across-track Resolution (m)	0.42	0.42	0.42
Along-track Resolution (m)	0.79	0.79	0.76

TABLE II: Transponder PTR values are presented for three processors: FF-WK Closed-Form, FF-WK Numerical and FF-BP. The processed time for all algorithms is 2.4 seconds.

the isardSAT's corner reflector located in Montsec (Catalonia) [23]. In this case, we have considered a processing time of 3.3 seconds in order to avoid aliasing in the Doppler frequencies. Figure 9 depicts the across and along-track cuts for a pass over the Corner Reflector the 25 October 2021. To better visualize of the across-track evolution, an oversampling factor of 8 has been applied. We can see that the shape of the sinc in the along-track dimension for the omega-K case is not perfect as in the transponder case. As the corner reflector Signal-to-Clutter is low compared to the transponder, the received energy for the point target is lower, making the phase of the received signal more noisy, and making it more difficult to the omega-K algorithm to obtain the expected sinc shape as predicted by the theory due to the approximations made for the algorithm, as the real point target signal differs from the theoretical model. However, the response of the point target is still clearly visible. Quantitatively, the PSLR for the across-track cut is measured at 11.5 dB and 14.8 dB, for the left and right lobes respectively. The width of the main lobe at -3 dB is 0.42 m. On the other hand, the left secondary lobe in the along-track cut reaches 13.2 dB and the right secondary lobe reaches 14.31 dB. The width of the main lobe at -3dB is 0.65 m, which represents a loss of 14% in the along-track theoretical resolution (0.57 m). In this case, the FF-WK numerical approach improves the performance of the closed-form algorithm, getting an along-track resolution of 0.63 m, which means a loss of 10.5% with respect to the theoretical. The backprojection algorithm gets closer to the

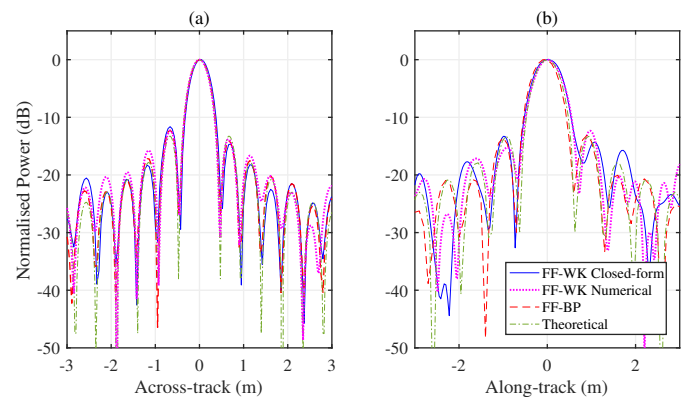


Fig. 9: PTR functions over the Corner reflector in Montsec corresponding the Sentinel-6 pass on October 25, 2021. The responses obtained by the FF-WK and FF-BP processors have been centered at the point of maximum power. (a) Across-track PTR. (b) Along-track PTR.

theoretical value, 0.6 m, representing a loss of only 5.3%. In contrast with the transponder case. The long-term behaviour is observed in Fig. 10, which depicts the evolution of the range bias between September 2021 and July 2022. In total, 28 passes has been processed. All of them were computed with the omega-K and the backprojection algorithms. For this study, the range samples have been over sampled by a factor of 128, which means that every sample is spaced 2.96 millimeters. The average range bias for the omega-K closed-form case is 2.99 cm and the standard deviation is 1.23 cm, while for the omega-K numerical processor the average range bias is 3.10 cm and the standard deviation is 1.22 cm. The average range bias for the backprojection case is 3.20 cm and the standard deviation is 0.93 cm, showing full consistency between methods and comparable precision. The approximately 3-centimeter range bias can be attributed to the residual uncertainty in the reflector vertex determination, as detailed in [23]. Refer to Table III for a comprehensive overview of all the obtained outcomes presented in this section. This table presents a summary of the results derived from the corner-reflector measurement campaign for both processors, encompassing both theoretical and empirical outputs. The parameters considered in this table include across-track and along-track resolution, peak-to-side lobe ratio, and range measurement stability.

### C. Distributed target: Open ocean

We have conducted an analysis of the performance of the FF-SAR omega-K algorithm over open ocean focusing on two well-known geophysical parameters: the Sea Surface Height (SSH) and the Significant Wave Height (SWH). The objective of this validation is to compare the results of FF-SAR algorithms (omega-K and backprojection) with the Sentinel-6 Mission Copernicus Operational L2 Product (delay/Doppler). Approximately 12 kilometers of Sentinel-6 data were processed: Three passes from 15 November 2021, 22 February 2022, and 14 January 2022, were selected in order to include a representative set of different Significant Wave Heights, from 2.6 to 4.1 m. The latitudes covered by these passes range between 25.0 and 28.6 deg.

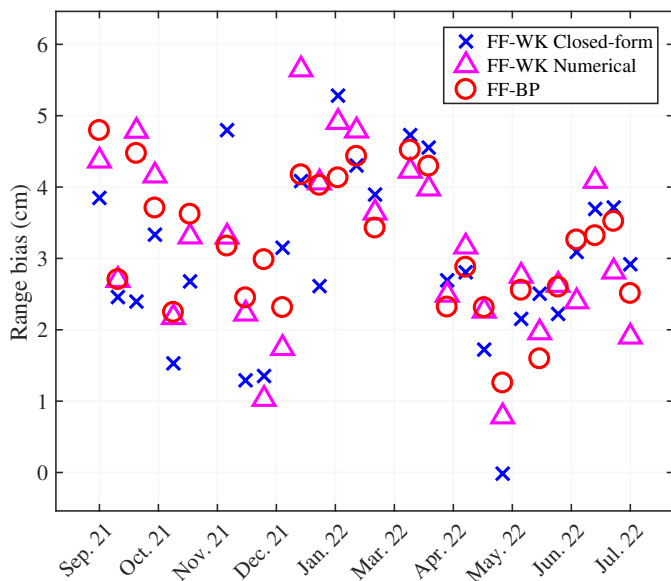


Fig. 10: Measured range bias with Sentinel-6 over the Montsec Corner Reflector computed with FF-WK closed-form, FF-WK numerical, and FF-BP processors during 1 year of measurements.

Corner Reflector	FF-WK CF	FF-WK NM	FF-BP
Range Bias STD (cm)	1.23	1.22	0.93
Range Bias Average (cm)	3.00	3.10	3.20
PSLR Left Across (dB)	11.5	11.90	11.90
PSLR Right Across (dB)	14.8	13.75	13.75
PSLR Left Along (dB)	13.20	15.20	13.75
PSLR Right Along (dB)	14.31	11.10	13.20
Across-track Resolution (m)	0.42	0.42	0.42
Along-track Resolution (m)	0.65	0.63	0.60

TABLE III: Corner Reflector range measurement stability values are presented for three processors: FF-WK Closed-Form, FF-WK Numerical and FF-BP. Range bias measurements were conducted for 28 passes between September 2021 and July 2022. The performance of PSLR and resolution has been done for a single pass that occurred the 25 October 2021.

The processing integration time was set to 2 s. The FF-SAR single look waveforms were multilooked in order to achieve a final spacing of 306 m in along-track, making these waveforms comparable to the DDP product. Finally, the range samples were oversampled by a factor of 2. The retracking stage was applied by adapting the delay/Doppler analytical retracker defined in [38] to operate with FF-SAR waveforms as done in [42]. This process was employed to derive the SSH and SWH for each spatial point.

After that, we proceeded to compute the standard deviation of SSH and SWH parameters as functions of the SWH. To achieve this, we calculate the standard deviations by averaging the variances of the obtained parameters from 20 consecutive power waveforms, known as the 20-Hz standard deviations. This calculation is performed after removing any trends and outliers present. Likewise, we determine the averages of the derived SWH, followed by sorting and grouping them into bins of 0.2 m each. Figure 11 showcases the standard deviation

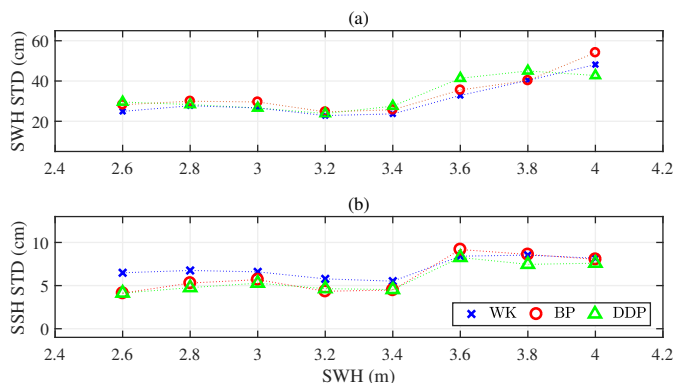


Fig. 11: Analysis of Sentinel-6 over an open ocean scenario: (a) Standard deviation of SWH and (b) Standard deviation of SSH as functions of SWH using FF-WK, FF-BP, and delay/Doppler methods. The standard deviation of SSH and SWH is consistent across all three approaches.

for both parameters in function of the SWH bins, showing consistent behaviour among all the processors.

## V. APPLICATIONS

The reduced execution time of FF-SAR omega-K algorithm in comparison to time-based backprojection processors, coupled with its enhanced along-track resolution compared to unfocused techniques like DDP, may be of interest for applications where vast extensions of data must be processed while maintaining high along-track resolution. In this section, we identify two specific applications: swell retrieval and sea ice monitoring.

### A. Swell retrieval

One of the primary goals of the Sentinel-6 mission is to monitor the evolution of the ocean over time, where radar altimetry is used to gather crucial geophysical parameters such as sea level and wind speed, among others. However, the vast size of the ocean poses a major challenge when processing large amounts data. Within this domain, one notable use is the monitoring of swell [43]. While swell retrieval using SAR techniques has been conducted for numerous years utilizing satellites like Sentinel-1 [44], observing swells through radar altimetry has been a pending research primarily due to the unique nadir-pointing geometry characteristic of radar altimeters, along with the restricted spatial resolution that existed prior to the development of FF-SAR algorithms. The utilization of fully-focused algorithms now permits the examination of swell waves through the analysis of intensity modulations in the waveform tail. Given that the geometry of radar altimetry diverges from that of other remote sensing systems such as conventional SAR, the interpretations and limitations associated with swell retrieval also differ significantly, ushering in new perspectives. Swell observations derived from altimetry hold significance as they enhance the spatial-temporal sampling of oceanic swell systems. Additionally, their monitoring aids in the cross-calibration of swell observations originating from various platforms [45]. In the context of radar altimetry, the monitoring of swells assumes a critical role in discerning

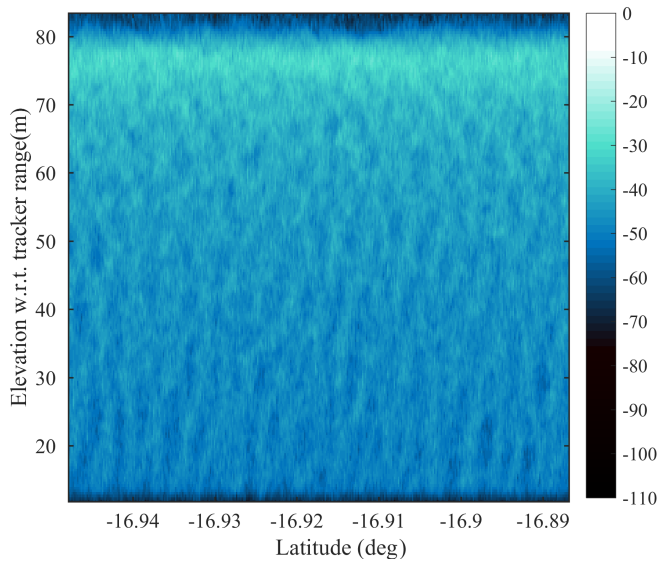


Fig. 12: FF-WK 2D image from an open ocean Sentinel-6 track. Swell-induced intensity modulations can be appreciated. Normalised power in decibels.

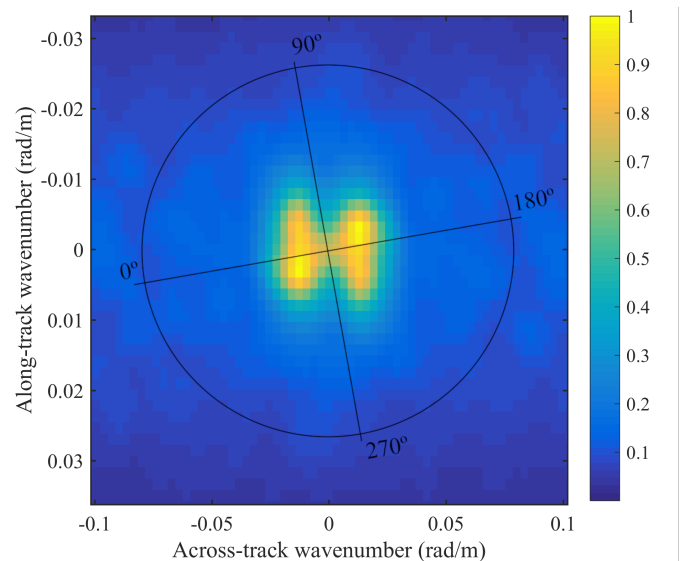


Fig. 13: FF-WK 2D cross-spectra. The ambiguities that appear in the image are due to the nature of the nadir-pointing antenna from the altimeter.

the influence of wind waves and swell within the sea-state bias [46]. Moreover, the process of swell-flagging plays a vital role in identifying potential biases present in retracers [47]. Recent work [28] has demonstrated the FF-SAR capabilities to map these spectra catching swell signals down to the meter scale. Additionally, ongoing projects like SARWAVE by the European Space Agency (ESA) [48] are currently involved in research efforts to provide a more detailed understanding of changes in swell intensity. This includes the incorporation of sublookng and its associated cross-spectra analysis, aimed at elevating the accuracy of retrieving swell-wave parameters.

In order to show the performance of the omega-K, a L1A Sentinel-6 product from the 25 May 2022, has been analysed. In this case, 2 s of processed time was utilized. Following the single-look processing, along-track focused points were multilooked at 30 m. Furthermore, range samples have been oversampled by a factor of 2. Figure 12 illustrates the two-dimensional response of an open ocean track with FF-WK. The ripples observed in along-track at the tails of the ocean waveforms are indicative of potential swell in the image. Without delving excessively into intricate details, Fig. 13 illustrates the 2D omega-K cross-spectra derived from the data shown in Fig. 12, following the methodology outlined in [28]. Preferably, we would like to have a single bright point indicating the direction of the swell. Instead, the 2D cross-spectra exhibit ambiguities in both directions, originated from the inherent characteristics of nadir-pointing antennas employed in altimeter systems. This design necessitates the altimeter to observe both sides of the ground track [28]. As an introduction to one of the potential applications of the omega-K processor, its capability to process open ocean scenarios with swell is presented, while acknowledging that further research is required to fully explore its capabilities in this area for the potential achievements of omega-K in swell retrieval applications.

### B. Sea ice Applications

Another application that involves the processing of large volume of data and will benefit from a high efficient FF-SAR algorithm is the sea ice monitoring. Sea ice applications, such as lead or iceberg detection, heavily rely on the utilization of high-resolution algorithms and computationally efficient processors to achieve optimal results. Although Sentinel-6 is not specifically designed to study ice scenarios in polar regions, an upcoming satellite mission, CRISTAL, will continue the primary objective of the CryoSat-2 mission and take advantage of an open burst scheme to produce high-resolution results [49].

For this analysis, a Sentinel-6 L1A product from the 5 September 2021 has been selected. The pass crosses latitudes between -65.05 and -65.01 degrees, near the Antarctic Peninsula. The data has been processed with the FF-SAR omega-K algorithm, using 2 s of processed time. After processing, the surface points has been averaged in order to obtain a multilooked surface of 30 m. Furthermore, range samples have been oversampled by a factor of 2. Figure 14 depicts a two-dimensional image processed with FF-WK for a sea ice scenario. As observed, leads can be easily distinguished from the ice zones due to the different backscatter energy of water compared to the energy reflected by ice. Leads can have dimensions in the order of a few meters, thus making high-resolution algorithms like backprojection and omega-K crucial for such applications. Figure 15 presents a comparison between the optical image and the FF-WK 2D radargram. The nadir-pointing orientation of the antenna introduces across-track ambiguities in the FF-WK 2D response, making it challenging to precisely geolocate leads within the same across-track range. However, prominent leads are clearly visible, and a correlation can still be established between the optical image and the leads detected in the altimeter radargram. The impact of the nadir-pointing antenna is evident in lead #1, as depicted

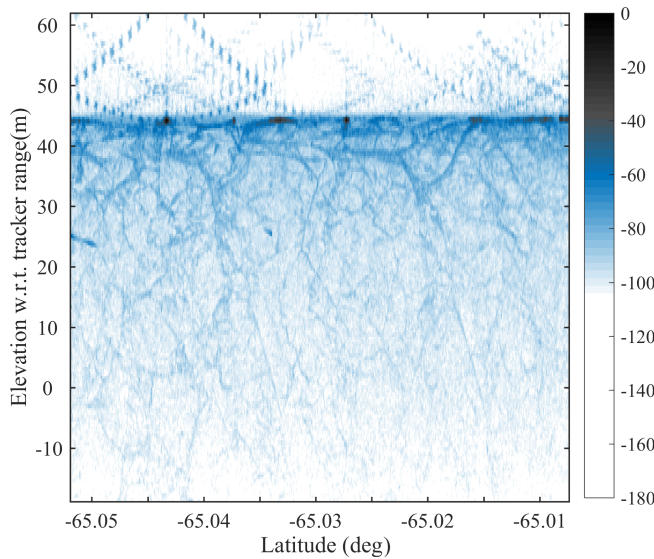


Fig. 14: FF-WK 2D Image from a sea ice Sentinel-6 track, where the distribution of off-nadir leads is clearly recognised. Normalised power in decibels. The parabolic features observed above the leading edge are caused by along-track replicas induced by periodic discontinuities in the pulse transmission chain for calibration purposes [16].

in Fig. 15. The radargram is illustrating an image of the latitude (x axis) and range (y axis), causing leads that intersect the track, like lead #1 mentioned earlier, to appear 'folded' in the two-dimensional altimeter radargram. It is essential to note that this limitation does not render certain applications impossible, and using image processing techniques should allow for high-resolution classification. For instance, water extent estimation from leads remains feasible [39]. Thanks to that, we can quantify the total amount of water surface and get better probability density functions of narrow leads, which is crucial to calibrate sea-ice models [50], [51], [52]. Additionally, successful lead detection and iceberg detection can still be achieved [29], [53]. Despite the challenges posed by across-track ambiguities, the data obtained from the FF-WK 2D radargram remains valuable for various analyses and studies related to sea ice monitoring and characterization.

## VI. COMPUTATIONAL EFFICIENCY

The main feature of the omega-K processor over the backprojection algorithm is the reduction in the number of operations required to obtain a single-look waveform. In the case of backprojection, the process involves compensating the phase of each received pulse and integrating them all in order to obtain a single-look waveform. In contrast, the omega-K processor necessitates the application of an FFT in the along-track direction and the use of a two-dimensional frequency filter to focus all the single-look waveforms covered during the processed time at once. This fundamental distinction yields a significant enhancement in computational efficiency. The number of operations that FF-SAR backprojection algorithm's requires to correct the phase of the two-dimensional waveforms and focus the data can be expressed in terms of the number of along-track points  $N_{ill}$  and the number of samples  $N_r$ , as shown in [26]:

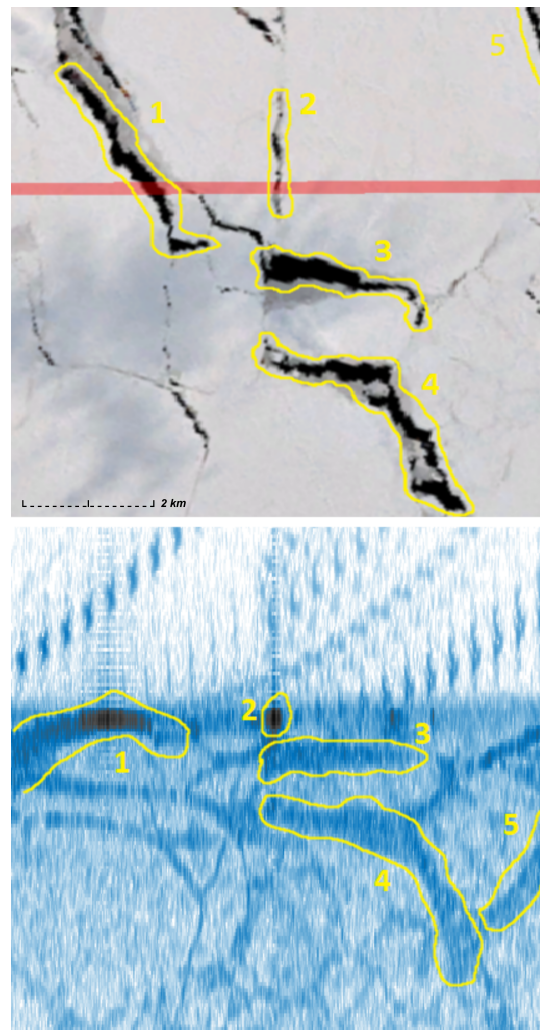


Fig. 15: Sentinel-2 image (top) and Sentinel-6 FF-WK 2D image (bottom) corresponding to a zoomed area of Fig. 14. Many of the leads in the optical image can be recognised in the altimeter radargram.

$$N_{BP} = N_{ill} \cdot (4 + \log_2 N_r). \quad (30)$$

For the omega-K processor, we have a data block containing  $N_{ill}$  echoes that are processed at once. Therefore, the number of operations required per sample and data block can be expressed as follows:

$$N_{WK} = 2 \cdot \left( \frac{N_p}{N_{ill}} + 1 + 2 \cdot \log_2 N_{ill} + \log_2 N_r \right). \quad (31)$$

In this context,  $N_p$  represents the number of operations required to compute essential input parameters such as equivalent velocity or Doppler rate. The computation of the equivalent velocity is straightforward and only needs 2-3 arithmetic operations for each data block. On the other hand, determining the Doppler rate requires about  $N_{ill}$  operations for each data block. Furthermore, the constant term of 1 accounts for the multiplication of the RFM filter with the two-dimensional frequency data. The second term corresponds to the Fast Fourier Transform (FFT) and Inverse FFT operations applied

to the along-track dimension. Lastly, the last term is for the range compression process at the end of the focusing. The multiplication factor of 2 applied to all operations originates from the presence of transient zones at the start and end of the data. These initial and final segments contain data points that cannot be entirely utilized for analysis, as the satellite's field of view does not encompass the complete observational dataset for those specific points. In this case, the FF-SAR omega-K processor has been designed in such way that half of the observed surface is erased in the end.

Just to provide an overview of the data scale we are handling, let us consider the case of Sentinel-6. During an processed time of 2 seconds, we have around 18,000 echoes of 256 range samples to process. In order to focus all the received pulses, approximately 216,000 operations are required for the FF-SAR backprojection processor, whereas for the omega-K closed-form algorithm only 74 operations are needed. For the case of the omega-K numerical approach, using [26, Eq. 16] with Sentinel-6 parameters, 922 operations are needed. This indicates that the FF-WK closed-form method requires around three thousand times less operations than the FF-BP processor, and around thirteen times less operations than the FF-WK numerical algorithm. It is important to note that the three algorithms could be optimized, for example using parallel computing, which means that the number of operations could be reduced. Even with that, the enhancement in the execution time of the omega-K method is quite significant. It is essential to note that in the backprojection algorithm, the number of operations increases linearly with the number of along-track pulses, whereas in the omega-K algorithm, the number of operations increases on a logarithmic scale. This implies that the omega-K algorithm becomes more efficient as we compute more surface, which is intuitive since the main objective of the FF-WK is to reduce the number of operations required to focus one data block of echoes simultaneously.

In order to compare the computational efficiency of both FF processors, a series of tests using a Sentinel-6 product pass over the corner-reflector with different configuration parameters has been done. The execution times for FF-WK and FF-BP with varying configurations are presented in Table IV. The tests have been done with an Intel(R) Core(TM) i7-4600M 2.90GHz single-core CPU with 16 GB of RAM. This experiment is presented to provide a general idea of the computational efficiency of both algorithms, as the results may vary depending on the code development, optimization techniques applied and the parallelisation strategy if any. The strong difference in terms of execution time is observed in all the tests, where the FF-WK is faster at least with a factor close to 2000 in the worst case. As we can observe in the second and third columns, reducing the along-track step size offers significant advantages to backprojection. By doing so, we effectively decrease the number of received pulses being processed. As mentioned earlier, the number of processed pulses directly impacts the number of operations required for backprojection, leading to a linear increase. Conversely, in the omega-K algorithm, this effect is logarithmic, resulting in a more gradual growth in processing operations with respect to the number of processed pulses. It's important to recall

<b>Parameters</b>				
Range zero-padding	1	1	1	2
Along-track step (m)	0.68	0.68	1.37	0.68
Observation Time (s)	1	2	2	2
Ground track length (km)	6	12	12	12
<b>Results</b>				
FF-WK execution time (s)	1.54	2.9	2.68	3
FF-BP execution time (s)	5520	10870	5515	11957

TABLE IV: Execution time of both FF processors for different testing parameters aimed at comparing the efficiency of the omega-K algorithm versus the classic backprojection alternative.

that these numbers may not align precisely with theoretical expectations due to various execution implications, including differences in code implementation for each processor.

## VII. DISCUSSION

The FF-SAR omega-K algorithm presented in this paper, validated with long series of point targets measurements, shows the viability of this kind of algorithms for future radar altimeter missions, and for the fast data reprocessing of current ones.

Assessing the results of range measurements using a Corner-Reflector, combined with observations taken from dispersed targets like the open ocean, provides important insights into the accuracy and precision capabilities of the omega-K system. As shown, the omega-K algorithm closely reproduces the results of the backprojection technique, showing slightly lower performance, while still being a good option for remote sensing purposes. The omega-K algorithm holds potential for a wide array of applications that were once limited by the slow computational performance of existing algorithms such as the backprojection. The reduction in execution time achieved by our algorithm unlocks opportunities for new applications. Specifically, this improved computational efficiency opens the door for the generation of global products in areas such as swell retrieval and sea ice, where time and precise data analysis is of importance. Also, other application such as global-scale in-land water processing, may benefit from fast algorithms [1], [18]. Finally, the almost real-time processing capability shown in Section VI with just a single CPU core opens the path for future in-flight real time processing of radar altimetry data, which holds interest for many of the applications introduced.

## VIII. CONCLUSION

The FF-SAR omega-K algorithm presented in this paper offers an alternative to current high-resolution radar altimetry algorithms such as the FF-SAR backprojection [17] and the 2D frequency domain [26].

The algorithm proposed has undergone a full validation process. The validation results over point targets, including simulated data and real data from a transponders and and

a corner reflector demonstrate a precision and an accuracy comparable to its equivalent time-domain alternative. Moreover, the results show the algorithm's versatility in various environments (open ocean and sea ice) and its potential applications, including a better estimation of swell, as well as lead and iceberg detection. Furthermore, it has been demonstrated that a two-dimensional frequency-based omega-K algorithm decreases substantially the execution time with respect to time-based processors such as the backprojection algorithm.

Finally, there are still potential areas for improvement and further investigation. Identifying limitations is crucial for improving the algorithm's performance and broadening its abilities. It is important to study how orbit assumptions affect the accuracy and precision of the algorithm. Additionally, we should conduct an analysis of how to optimize algorithm parameters such as the along-track windowing and the mitigation of replicas, taking into account the specific application and any limitations inherent to the algorithm. Moreover, we need to explore strategies for addressing issues such as the synchronization of the PRF changes to have equispaced data in each block of echoes that will be processed for the WK algorithm. In terms of applications, exploring specific application requirements is essential for enhancing the algorithm. Also, future research efforts should also concentrate on refining the implementation and optimization of the processor, as operational applications where global products are crucial poses a significant challenge in the future.

#### ACKNOWLEDGMENT

S.H. would like to express his gratitude to the Delft University of Technology (TU Delft) for hosting him during three months as part of his PhD. Also, we thank Ester Vendrell (isardSAT) for her advice during the writing phase of this document.

#### REFERENCES

- [1] S. Vignudelli, A. Scozzari, R. Abileah, J. Gómez-Enri, J. Benveniste, and P. Cipollini, "Chapter Four - Water surface elevation in coastal and inland waters using satellite radar altimetry," in *Extreme Hydroclimatic Events and Multivariate Hazards in a Changing Environment*, V. Maggioni and C. Massari, Eds. Elsevier, 2019, pp. 87–127.
- [2] A. Tarpanelli and J. Benveniste, "Chapter Eleven - On the potential of altimetry and optical sensors for monitoring and forecasting river discharge and extreme flood events," in *Extreme Hydroclimatic Events and Multivariate Hazards in a Changing Environment*, V. Maggioni and C. Massari, Eds. Elsevier, 2019, pp. 267–287.
- [3] K. A. Giles, S. W. Laxon, and A. P. Worby, "Antarctic sea ice elevation from satellite radar altimetry," *Geophysical Research Letters*, vol. 35, no. 3, 2008. [Online]. Available: <https://agupubs.onlinelibrary.wiley.com/doi/abs/10.1029/2007GL031572>
- [4] A. Mémin, T. Flament, F. Rémy, and M. Llubes, "Snow- and ice-height change in Antarctica from satellite gravimetry and altimetry data," *Earth and Planetary Science Letters*, vol. 404, pp. 344–353, 2014.
- [5] A. Cazenave, H. Palanisamy, and M. Ablain, "Contemporary sea level changes from satellite altimetry: What have we learned? What are the new challenges?" *Advances in Space Research*, vol. 62, no. 7, pp. 1639–1653, 2018.
- [6] L. Gray, D. Burgess, L. Copland, T. Dunse, K. Langley, and G. Moholdt, "A revised calibration of the interferometric mode of the CryoSat-2 radar altimeter improves ice height and height change measurements in western Greenland," *The Cryosphere*, vol. 11, pp. 1041–1058, 2017.
- [7] M. Grgić and T. Bašić, *Radar Satellite Altimetry in Geodesy -Theory, Applications and Recent Developments*, 2021, pp. 1–18.

- [8] CryoSat-2 Mission Summary. Accessed: 7 December 2023. [Online]. Available: <https://www.eportal.org/satellite-missions/cryosat-2#preparatory-campaigns>
- [9] Sentinel-3 Mission Summary. Accessed: 7 December 2023. [Online]. Available: <https://sentinels.copernicus.eu/web/sentinel/missions/sentinel-3/overview/mission-summary>
- [10] Sentinel-6 Mission Summary. Accessed: 7 December 2023. [Online]. Available: <https://sentinels.copernicus.eu/web/sentinel/missions/sentinel-6/overview>
- [11] R. K. Raney, "The Delay/Doppler Radar Altimeter," *IEEE*, vol. 36, no. 5, pp. 1578–1588, 1998.
- [12] C. Donlon, R. Cullen, L. Giulicchi, M. Fornari, and P. Vuilleumier, "Copernicus Sentinel-6 Michael Freilich Satellite Mission: Overview and Preliminary in Orbit Results," in *2021 IEEE International Geoscience and Remote Sensing Symposium IGARSS*, 2021, pp. 7732–7735.
- [13] K. R. Raney, "CryoSat SAR-Mode Looks Revisited," in *ESA Living Planet Symposium*, ser. ESA Special Publication, H. Lacoste-Francis, Ed., vol. 686, 2010, p. 216.
- [14] R. K. Raney, "Maximizing the Intrinsic Precision of Radar Altimetric Measurements," *IEEE Geoscience and Remote Sensing Letters*, vol. 10, no. 5, pp. 1171–1174, 2013.
- [15] C. Gommenginger, C. Martin-Puig, A. Laiba, and R. Raney, "Review of state of knowledge for SAR altimetry over ocean. Report of the EUMETSAT JASON-CS SAR mode error budget study," 2013.
- [16] S. Amraoui *et al.*, "FFSAR Replica Removal Algorithm For Closed-Burst Data," 2022, oral presentation.
- [17] A. Egado and W. H. F. Smith, "Fully Focused SAR Altimetry: Theory and Applications," *IEEE*, vol. 55, no. 1, pp. 392–406, 2017.
- [18] M. Kleinherenbrink, M. Naeije, C. Slobbe, A. Egado, and W. Smith, "The performance of CryoSat-2 fully-focussed SAR for inland water-level estimation," *Remote Sensing of Environment*, vol. 237, p. 111589, 2020.
- [19] Y. Yuan, "Estimation of River Width with Fully-Focused SAR Altimetry Data," in *AGU Fall Meeting Abstracts*, 2019.
- [20] F. Schlembach *et al.*, "Benefits of Fully Focused SAR Altimetry to Coastal Wave Height Estimates: A Case Study in the North Sea," 2022.
- [21] H. C. Team, "HCA Impact Assessment Report," 2023.
- [22] A. Egado, D. C. Vandemark, and H. Feng, "An Evaluation of Fully Focused SAR Altimetry for Coastal Applications," in *AGU Fall Meeting Abstracts*, vol. 2018, 2018, pp. OS43A–04.
- [23] F. Gibert *et al.*, "A Trihedral Corner Reflector for Radar Altimeter Calibration," *IEEE Transactions on Geoscience and Remote Sensing*, vol. 61, pp. 1–8, 2023.
- [24] L. Ulander, H. Hellsten, and G. Stenstrom, "Synthetic-aperture radar processing using fast factorized back-projection," *IEEE Transactions on Aerospace and Electronic Systems*, vol. 39, no. 3, pp. 760–776, 2003.
- [25] A. Fasih and T. Hartley, "Gpu-accelerated synthetic aperture radar backprojection in cuda," in *2010 IEEE Radar Conference*, 2010, pp. 1408–1413.
- [26] P. Guccione, M. Scagliola, and G. Davide, "2D Frequency Domain Fully Focused SAR Processing for High PRF Radar Altimeters," *Remote Sensing*, vol. 10, no. 12, p. 1943, 2018.
- [27] M. Scagliola, P. Guccione, and D. Giudici, "Fully Focused SAR Processing for Radar Altimeter: a Frequency Domain Approach," in *IGARSS 2018 - 2018 IEEE International Geoscience and Remote Sensing Symposium*, 2018, pp. 6699–6702.
- [28] O. Altiparmaki, M. Kleinherenbrink, M. Naeije, C. Slobbe, and P. Visser, "SAR Altimetry Data as a New Source for Swell Monitoring," *Geophysical Research Letters*, vol. 49, no. 7, p. e2021GL096224, 2022.
- [29] D. Dettmering, A. Wynne, F. L. Müller, M. Passaro, and F. Seitz, "Lead Detection in Polar Oceans—A Comparison of Different Classification Methods for Cryosat-2 SAR Data," *Remote Sensing*, vol. 10, p. 1190, 2018.
- [30] I. G. Cumming and F. H. Wong, *Digital Processing of Synthetic Aperture Radar Data: Algorithms and Implementation*. Artech House, 2005.
- [31] J. MacArthur, "Design of the SEASAT-A Radar Altimeter," in *OCEANS '76*, 1976, pp. 222–229.
- [32] H. Breit, T. Fritz, U. Bals, M. Lachaise, A. Niedermeier, and M. Vonavka, "Terrasar-x sar processing and products," *IEEE Transactions on Geoscience and Remote Sensing*, vol. 48, no. 2, pp. 727–740, 2010.
- [33] J.-W. Park and J.-S. Won, "An efficient method of doppler parameter estimation in the time–frequency domain for a moving object from terrasar-x data," *IEEE Transactions on Geoscience and Remote Sensing*, vol. 49, no. 12, pp. 4771–4787, 2011.
- [34] C. J. Donlon *et al.*, "The Copernicus Sentinel-6 mission: Enhanced continuity of satellite sea level measurements from space," *Remote Sensing of Environment*, vol. 258, p. 112395, 2021.

- [35] C. Bender, S. Orszag, and S. Orszag, *Advanced Mathematical Methods for Scientists and Engineers I: Asymptotic Methods and Perturbation Theory*, ser. Advanced Mathematical Methods for Scientists and Engineers. Springer, 1999.
- [36] S. Dinardo *et al.*, "Sentinel-6 MF Poseidon-4 Radar Altimeter In-Flight Calibration and Performances Monitoring," *IEEE Transactions on Geoscience and Remote Sensing*, vol. 60, pp. 1–16, 2022.
- [37] M. Kuschnerus *et al.*, "Sentinel-6 poseidon-4 rmc mode processing and expected performance," OSTST, 2018.
- [38] C. Ray *et al.*, "SAR Altimeter Backscattered Waveform Model," *IEEE Transactions on Geoscience and Remote Sensing*, vol. 53, no. 2, pp. 911–919, 2015.
- [39] F. L. Müller, D. Dettmering, W. Bosch, and F. Seitz, "Monitoring the Arctic Seas: How Satellite Altimetry Can Be Used to Detect Open Water in Sea-Ice Regions," *Remote Sensing*, vol. 9, no. 6, 2017.
- [40] S. Mertikas *et al.*, "A permanent infrastructure in Crete for the calibration of Sentinel-3, Cryosat-2 and Jason missions with a transponder," in *Proceedings of the ESA Living Planet Symposium*, 2013.
- [41] S. Amraoui *et al.*, "New results of Sentinel-6 transponder working group," in *3rd Sentinel-6 Validation Team Meeting*, 2021.
- [42] F. Gibert *et al.*, "Results of the Dragon 4 Project on New Ocean Remote Sensing Data for Operational Applications," *Remote Sensing*, vol. 13, no. 14, 2021.
- [43] F. Collard, F. Ardhuin, and B. Chapron, "Monitoring and analysis of ocean swell fields from space: New methods for routine observations," *Journal of Geophysical Research: Oceans*, vol. 114, no. C7, 2009.
- [44] H. Wang, A. Mouche, R. Husson, and B. Chapron, "Dynamic Validation of Ocean Swell Derived from Sentinel-1 Wave Mode Against Buoys," in *IGARSS 2018 - 2018 IEEE International Geoscience and Remote Sensing Symposium*, 2018, pp. 3223–3226.
- [45] Y. W. Yanmin Zhang and Q. Xu, "On the Nonlinear Mapping of an Ocean Wave Spectrum into a New Polarimetric SAR Image Spectrum," *Journal of Physical Oceanography*, vol. 50, no. 11, pp. 3109–3122, 2020.
- [46] F. Collard, L. Marié, F. Nouguié, M. Kleinherenbrink, F. Ehlers, and F. Ardhuin, "Wind-Wave Attenuation in Arctic Sea Ice: A Discussion of Remote Sensing Capabilities," *Journal of Geophysical Research: Oceans*, vol. 127, no. 7, p. e2022JC018654, 2022.
- [47] F. Schlembach *et al.*, "Round Robin Assessment of Radar Altimeter Low Resolution Mode and Delay-Doppler Retracking Algorithms for Significant Wave Height," *Remote Sensing*, vol. 12, no. 8, 2020.
- [48] SARWAVE project. Accessed: 7 December 2023. [Online]. Available: <https://www.sarwave.org/>
- [49] M. Kern *et al.*, "The Copernicus Polar Ice and Snow Topography Altimeter (CRISTAL) high-priority candidate mission," *The Cryosphere*, vol. 14, no. 7, pp. 2235–2251, 2020.
- [50] A. Herman, M. Wenta, and S. Cheng, "Sizes and Shapes of Sea Ice Floes Broken by Waves—A Case Study From the East Antarctic Coast," *Frontiers in Earth Science*, vol. 9, 2021.
- [51] A. A. Denton and M.-L. Timmermans, "Characterizing the sea-ice floe size distribution in the Canada Basin from high-resolution optical satellite imagery," *The Cryosphere*, vol. 16, 2022.
- [52] T. W. Armitage and R. Kwok, "SWOT and the ice-covered polar oceans: An exploratory analysis," *Advances in Space Research*, vol. 68, no. 2, pp. 829–842, 2021.
- [53] J. Tournadre, N. Bouhier, F. Boy, and S. Dinardo, "Detection of iceberg using Delay Doppler and interferometric Cryosat-2 altimeter data," *Remote Sensing of Environment*, vol. 212, pp. 134–147, 2018.

**Sergi Hernandez** received the M.S. degree in Telecommunications Engineering from the Universitat Politècnica de Catalunya, Barcelona, in 2020. He is currently pursuing his Ph.D. degree in signal theory and communications at the Universitat Politècnica de Catalunya, Barcelona, co-directed by isardSAT-Cat, Barcelona. In 2019, he joined isardSAT as a Research and Development Engineer. His main activities are the research, development, and implementation of altimetry data processing algorithms.

**Ferran Gibert** received the M.S. degree in aerospace engineering and the Ph.D. degree in aerospace science and technology from the Universitat Politècnica de Catalunya, Barcelona, in 2011 and 2016, respectively. His Ph.D. was focused on the design of thermal diagnostics experiments for the LISA Pathfinder mission. From 2016 to 2018, he completed a post-doctoral research with the University of Trento, Trento, Italy, from where he supported the LISA Pathfinder operations and data analysis phase. Since June 2018, he has been a Research and Development Engineer with isardSAT, Barcelona, being currently involved in the development of algorithms for radar altimeter processors.

**Antoni Broquetas** (S'84–M'90) was born in Barcelona, Catalonia, in 1959. He received the Engineering and Doctor Engineering degrees in telecommunication engineering from the Universitat Politècnica de Catalunya (UPC), Barcelona, in 1985 and 1989, respectively, where his dissertation was on microwave tomography. In 1986, he was a Research Assistant with Portsmouth Polytechnic, Portsmouth, U.K., where he was involved in propagation studies. In 1987, he joined the Department of Signal Theory and Communications, School of Telecommunication Engineering, UPC. From 1998 to 2002, he was the Subdirector of Research at the Institute of Geomatics, Barcelona. Since 1999, he has been a Full Professor with the UPC, where he is involved in research on radar imaging and remote sensing. From 2003 to 2006, he was the Director of the Department of Signal Theory and Communications, UPC. From 2005 to 2009, he proposed and managed the Knowledge To Market (K2M) Program at UPC to support university spin-offs. He has published more than 200 papers on microwave tomography, radar, ISAR and synthetic aperture radar (SAR) systems, SAR processing, and interferometry. His present research interest includes SAR calibration techniques, GMTI SAR performance analysis, GEOSAR, and mmW ground-based SAR, in support of future SAR missions and radar remote sensing innovation.

**Marcel Kleinherenbrink** received the master's degree from the Faculty of Aerospace Engineering, Delft University of Technology, Delft, The Netherlands, in 2013, and the Ph.D. degree from the Faculty of Civil Engineering and Geoscience, Delft University of Technology, in 2018, with a focus on the observation of sea-level change and vertical land motion from space. He specializes in the observation of the ocean surface using active radar instruments. In 2019, he became involved in the Earth Explorer 10 Mission, Harmony, for which he implements forward models, investigates inversion strategies, and provides performance estimates. Since 2018, he has been involved in numerous European Space Agency (ESA) projects related to future missions and novel retrieval algorithms for ocean observations.

**Adrián Flores de la Cruz** received the M.S. and Ph.D. degrees in telecommunications engineering from the Polytechnic University of Cartagena, Murcia, Spain, in 2014 and 2019, respectively. From 2017 to 2019, he was with Hisdesat SA, Madrid, Spain, as a Cal/Val Engineer, where he worked on the PAZ Mission. Since March 2019, he has been a Research and Development Engineer with isardSAT, Barcelona, working on the development and implementation of data processing techniques with special focus on the instrumental calibration.

**Adrià Gómez-Olivé** received the bachelor's degree in telecommunications technologies and services engineering from the Universitat Politècnica de Catalunya, Barcelona, in 2022, where he is currently pursuing the M.S. degree in advanced telecommunication technologies. He joined isardSAT-Cat, Barcelona, in 2021. His tasks include the implementation and handling of processing techniques of SAR altimetry data for calibration and monitoring tools and the analysis of inland water level and extension from altimetry data measurements.

**Albert Garcia-Mondéjar** received the M.S. degree in telecommunications engineering from the Universitat Politècnica de Catalunya, Barcelona, in 2009. He joined isardSAT-Cat, Barcelona, in 2011, where he is currently a Senior Altimetry Engineer and the Research and Development Manager. He lead isardSAT-UK, Guildford, from 2014 to 2019. He has wide experience in algorithm development, from L0 to L2, for SAR altimetry missions. His fields of expertise include the improvement of L1 algorithms, instrument calibration, science multimission activities, and innovative methods to improve performances over complex scenarios.

**Mònica Roca i Aparici** received her M.S. degree in Electronics and Telecommunication Engineering from the Universitat Politècnica de Catalunya, Barcelona, Catalonia, in 1995. She is the Founder and Director of isardSAT Group since its foundation in 2006. She has been actively involved in the design and development of on-board and on-ground processing algorithms (including instrument calibration, Level 1 processing, and up to Level-2 retracking algorithms) mainly from radar altimetry instruments on-board ESA satellites and in all satellite mission phases, and for all ESA Earth Observation missions which embark a radar altimeter, for more than 25 years. She also worked at ESA/ESTEC from 1994 until 2003 as a radar performance engineer of EnviSat RA-2.